Article

High-Throughput Screening of Nitrogen-Coordinated Bimetal Catalysts for Multielectron Reduction of CO_2 to CH_4 with High Selectivity and Low Limiting Potential

Shuo Wang, Lei Li,* Jing Li, Chengzong Yuan, Yao Kang, Kwan San Hui,* Jintao Zhang, Feng Bin, Xi Fan, Fuming Chen,* and Kwun Nam Hui*

Read Online

ACCESS | Metrics & More | Article Recommendations | Supporting Information

ABSTRACT: Significant challenges remain for developing efficient catalysts in an electrochemical multielectron CO_2 reduction reaction (CO_2RR), which usually suffers from poor activity and selectivity. Motivated by the recent experimental progress in fabricating dual-metal atom catalysts (DMACs) in N-doped graphene materials (graphene-N6V4; N: nitrogen and V: vacancy), we sampled eight types of homonuclear (N6V4-M_2, M = Cr, Mn, Fe, Co, Ni, Cu, Pd, and Ag) catalysts and 28 types of heteronuclear (N6V4-M1M2) catalysts to study CO_2RR activity via first-principles high-throughput screening. Using stability, activity, and selectivity as indicators along with the broken conventional scaling relationship, N6V4-AgCr was selected as a promising candidate for deep CO_2 reduction to methane with a low overpotential of 0.55 V after two screening rounds. Further analysis showed that a frustrated Lewis pair, formed between metal and the para-N, owing to the difference in the electronic arrangement of the d orbitals of various transition metals, caused a difference in the spin polarization of the systems and affected the catalytic performance of each DMAC. Our work not only provides a solid strategy for screening potential catalysts but also demonstrates that their CO_2 reduction activities originate from the various atomic and electronic structures of DMACs.
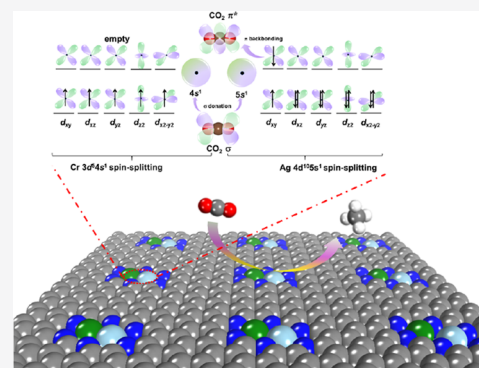
1. INTRODUCTION

The growing demand for fossil fuels is accompanied by excessive emissions of CO_2, resulting in severe climate change with harmful impacts on the environment and health. Thus, there is an urgent need to seek effective methods for reducing CO_2 content, converting CO_2 into fuels, and further closing the anthropogenic C cycle. The electrochemical CO_2 reduction reaction (CO_2RR) is regarded as a promising approach for managing the global C balance and converting CO_2 into value-added C-based products.[1,2] In particular, CO_2RR can produce several C1 products including carbon monoxide (CO), formic acid (HCOOH), methanol (CH_3OH), and methane (CH_4). All of the C1 products are highly relevant to the chemical industry.[3−5] However, previous studies mainly focused on the two-electron reduction process, such as the reduction of CO_2 to CO or HCOOH.[6−9] The practical implementation of multielectron reduction of CO_2 faces major hurdles due to energy efficiency and product selectivity.[10,11] In this regard, exploring robust catalysts for deep CO_2 reduction with high activity and selectivity is still a truly novel undertaking.[12]

Transition metals (denoted M) are the most common choice for CO_2RR electrocatalysts. To date, Cu-based materials have been demonstrated as the most widely investigated metal catalysts for CO_2 reduction toward deeper reduction products.[10,13] However, the conventional linear scaling relations between the adsorption strengths of reaction intermediates on the pure metal surface greatly limit the exploration of superior catalysts toward other metal catalysts.[14,15] Generally, pure metal materials cannot effectively activate CO_2 due to the scaling relations unless a prohibitively high overpotential of −1 V is used to initiate the reaction.[16] In addition, the hydrogen evolution reaction (HER) can easily dominate under the same conditions, decreasing the efficiency of CO_2RR.[2,17,18] Therefore, a widespread approach is to perform an atomic-level manipulation of metal atoms for designing highly active electrocatalysts. To solve the problems of reactivity and selectivity, recently, some single-atom catalysts (SACs) have been widely studied.[19,20] However, the catalytic activity of a single-atom catalyst is usually limited to the low density of the metal active site, coupled with a relatively simple electronic structure.[21] Meanwhile, the single-
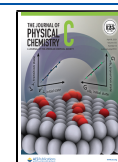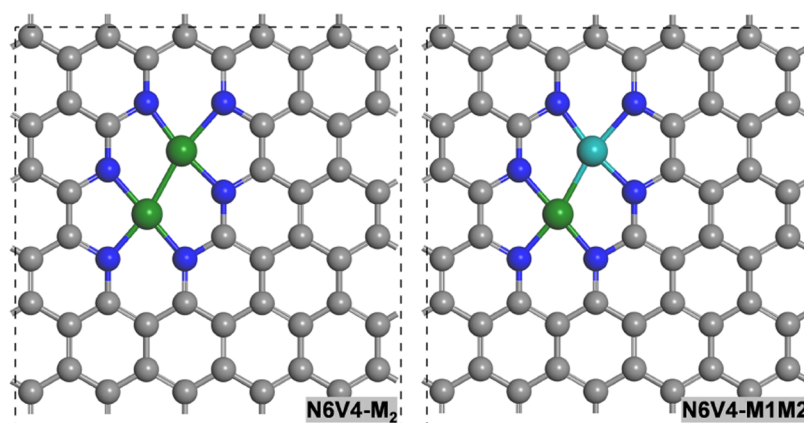
Figure 1. Schematic of the geometric structure of N6V4-M$_2$ and N6V4-M1M2. The gray and blue balls represent C and N atoms, respectively, and the cyan and green balls represent the two transition-metal atoms.

metal atoms tend to form clusters during synthesis, leading to challenges in efficient use of single-atom catalysts.[22,23]

In this case, dual-metal atom catalysts (DMACs), with M1M2−N$_x$−C coordination, have received considerable attention in heterogeneous catalysis because of their unique atomic and electronic structures compared to SACs. DMACs exert mutual effects for tuning the electronic structures of both M sites, altering the binding energy of reaction intermediates. Such effects reduce the energy barrier and improve the reaction rate through an efficient and stable approach.[24−26] The electrochemical applications of DMACs have been used toward multi-intermediate electrochemical reactions, such as the oxygen reduction/evolution reaction (ORR/OER),[27−30] CO$_2$RR,[26,31−34] and N$_2$ reduction reaction (NRR).[35−37] In the applications of the CO$_2$RR field, several researchers have successfully prepared DMACs in C-based materials and suggested DMACs as a potential alternative to Cu as electrocatalysts for CO$_2$RR.[30,38−43] For example, Ren et al. synthesized a novel electrocatalyst with Fe−Ni dual sites embedded into N-doped porous C as an efficient catalyst for CO$_2$RR.[44] By utilizing the strong adsorption of CO$_2$ molecules on Fe and the weak binding capacity of Ni with CO, the selectivity of the DMAC for CO$_2$RR toward CO achieves an impressive high selectivity of 99%; the Faraday efficiency (FE) exceeds 90% in a wide potential range, ranging from −0.5 to −0.9 V, reaching 98% at −0.7 V compared with a reversible hydrogen electrode (RHE). Two recent studies also successfully identified high-activity catalysts for CO$_2$RR by breaking down the severe restriction imposed by scaling relations on catalytic activity.[26,34] Significant activity and selectivity for CO have also been observed in Cu/Mn, Ni/Mn, and Ni/Fe DMACs via theoretical computations. The results are even better than that of the well-established metal catalyst due to the breaking of the scaling relationship between the adsorption strength of *CO and *COOH species (* indicates the active site).[34] Despite their superior activity, some questions regarding DMACs remain unanswered. First, given that the combination of two different transition-metal atoms has many possibilities, can theoretical calculations screen out experimentally unexplored DMACs with remarkable CO$_2$RR catalytic performance? Second, what are the fundamental factors that determine the catalytic activity of DMACs? Answering these questions can identify potential good catalysts for CO$_2$RR and provide guidelines for designing highly

efficient DMACs for CO$_2$RR and other electrochemical reactions.

In this work, high-throughput density functional theory (DFT) calculations were conducted to investigate several transition-metal (M = Cr, Mn, Fe, Co, Ni, Cu, Pd, and Ag) homonuclear and heteronuclear dual-metal atoms embedded into a series of N-doped graphene-based catalysts (denoted N6V4-M$_2$ or N6V4-M1M2, as shown in Figure 1). Half of the candidates were first selected by evaluating stability, activity, and selectivity. Further analysis was performed by breaking the scaling relationship between the adsorption strengths of *COOH/*CHO and *CO species. Then, N6V4-AgCr was identified from the 36 concept catalysts as a highly promising catalyst for the electrochemical CO$_2$ reduction to produce CH$_4$. Additional investigation showed that a frustrated Lewis pair (FLP) was formed between the metal and the adjacent N due to the different spin polarizations in the electronic arrangement of the d orbitals of various transition metals. The catalytic performance was significantly dominated by the various spin polarizations of the screened systems.

2. MODELS AND COMPUTATIONAL METHODS

2.1. Models. Based on the experimental characterization results of the K-edge X-ray absorption near-edge structure and the extended X-ray absorption fine structure spectra,[39] a rectangular superlattice of graphene to confine a pair of metal atoms with coordinated N was considered. As shown in Figure 1, two transition-metal atoms are joined in graphene to replace four C vacancies, and both atoms are surrounded by three N atoms. Hence, we define it as N6V4-M$_2$/M1M2. Geometrically, M1 and M2 are equivalent sites, and thus, 28 heteronuclear N6V4-M1M2 and 8 homonuclear N6V4-M$_2$ were calculated in our work.

2.2. Computational Methods. All of the calculations were performed on the basis of the spin-polarized DFT[45] methods implemented in the Vienna Ab initio Simulation Package (VASP 6.0).[46] The generalized gradient approximation was used to estimate the exchange−correlation interaction[47] in the scheme of the Perdew−Burke−Ernzerhof functional.[48] The effect of core electrons on the density of valence electrons was described using the projector augmented wave method.[49] The kinetic energy cutoff for the plane waves was set to 450 eV for all of the calculations in the 6 × 6 × 1 graphene supercells. The convergence tolerances of energy and force on each atom during structure relaxation were less than
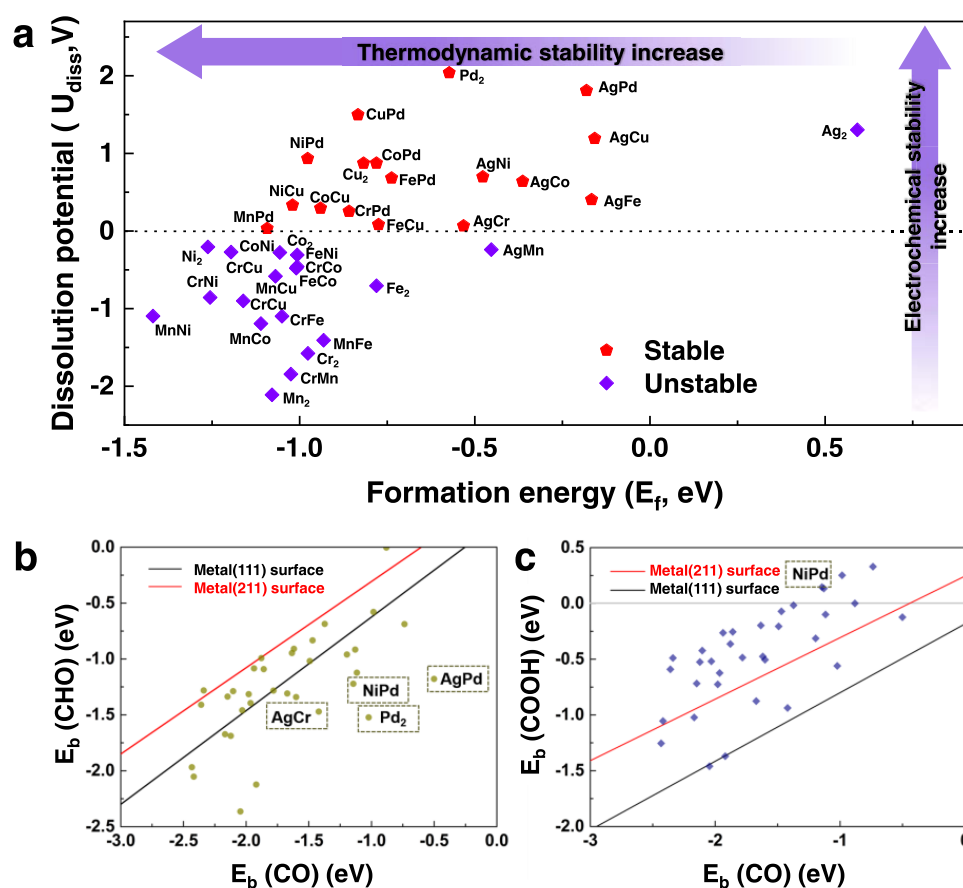
Figure 2. (a) Computed formation energy and dissolution potential of metal atoms in N6V4-M_2/M1M2. (b, c) Relationship between the binding energies of (b) E_b(CHO) and E_b(CO) and (c) E_b(COOH) and E_b(CO) of the N6V4-M_2/M1M2 systems on the transition-metal surface. The calculated Ni, Cu, Ag, Pd, Au, Pt, and Rh data was used to generate a linear proportional relationship between adsorbates.[55]

10^{-4} eV and 0.02 eV/Å, respectively. A set of Monkhorst–Pack mesh K points of $3 \times 3 \times 1$ and $5 \times 5 \times 1$ is used to sample the Brillouin zone for geometry optimization and electronic structural calculations.[50] A vacuum distance of 20 Å was set for graphene to ensure sufficient vacuum and avoid interactions between two periods. The thermal and zero-point energy (ZPE) corrections of different C intermediates adsorbed onto graphene were further calculated at the Γ point. Grimme's dispersion-corrected DFT scheme was used to describe the van der Waals interactions in the systems.[51,52]

The free energy (G) of each reaction intermediate is given as $G = E_{DFT} + E_{ZPE} - TS$, where E_{DFT} is the DFT calculated electronic energy and E_{ZPE} and S are the ZPE correction and the entropy, respectively. T is the temperature and it was set to 298.15 K. At electrode potential $U = 0$ V (versus RHE), the change of free energy (ΔG) can be calculated using the following equation: $\Delta G = \Delta E + \Delta ZPE - T\Delta S$, where ΔE is the reaction energy of hydrogenation and ΔE_{ZPE} and ΔS are the differences of E_{ZPE} and S, respectively. The E_{ZPE} and TS for all of the intermediates of CO_2 reduction on N6V4-M_2/M1M2 are calculated by the following equations

$$E_{ZPE} = \frac{1}{2} \sum_i h\nu_i \tag{1}$$

$$-TS = K_B T \sum_i \ln(1 - e^{-h\nu_i/K_B T}) - \sum_i h\nu_i \left(\frac{1}{e^{h\nu_i/K_B T} - 1}\right) \tag{2}$$

where h, ν, and K_B represent the Planck constant, vibrational frequencies, and the Boltzmann constant, respectively.

3. RESULTS AND DISCUSSION

3.1. Stability and Screening Methods. First, we theoretically examine the geometric structures of the aforementioned 8 homonuclear N6V4-M_2 and 28 heteronuclear N6V4-M1M2 monolayers. The details of the optimized structures are provided in Figure S1 of the Supporting Information. All metal atoms can be incorporated into the central cavity of graphene and form nearly in-plane configurations. The distances between two metal atoms are within the range of 2.19 Å (for N6V4-FeCo) to 2.53 Å (for N6V4-CrMn). All metal dimers exhibit shorter bond length compared with the interatomic bond length in their bulk. This interconnection enables electronic conversion between dimers to synergistically react and adsorb the adsorbate, triggering a different catalytic performance from the monoatomic counterpart.[53]

Then, we evaluated the thermodynamic and electrochemical stabilities of the 36 N6V4-M_2/M1M2 monolayers through their formation energy E_f and dissolution potential U_{diss} (Figure 2a),[54] which are defined as $E_f = (E_{total} - E_{N6V4} - 2E_M)/2$ and $U_{diss} = U°_{diss}(\text{metal } 1, \text{bulk}) + U°_{diss}(\text{metal } 2, \text{bulk}) - \frac{E_f}{n1e + n2e}$ for homonuclear, where E_M is the total energy of the metal atoms in the most stable bulk structure, E_{total} and E_{N6V4} are the total energies of N6V4-M_2/M1M2 and the substrate,
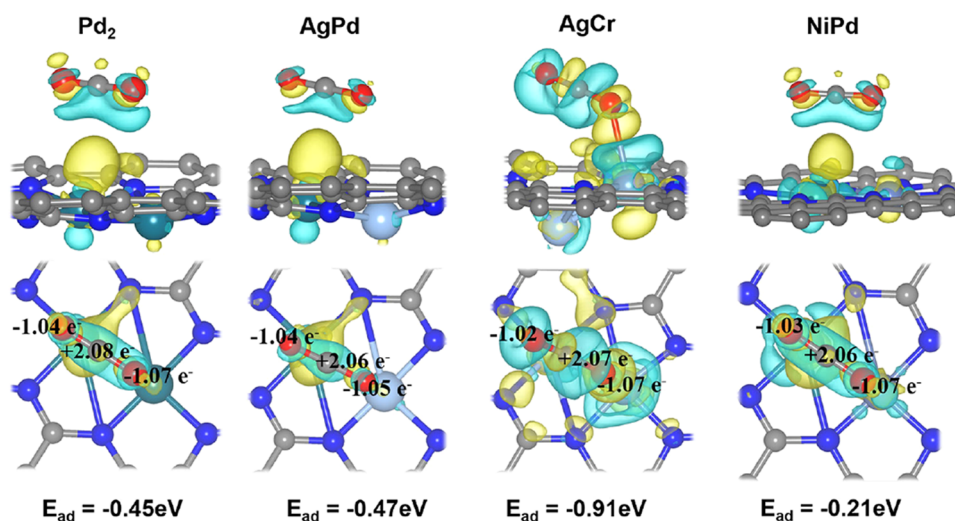
Figure 3. Side and top views of the charge density difference for CO_2 adsorbed on N6V4-M_2/M1M2 (N6V4-Pd_2, N6V4-AgCr, N6V4-AgPd, and N6V4-NiPd). In the lower panel, negative values indicate the number of obtained electrons, and positive values indicate the number of lost electrons. Charge depletion and accumulation are presented in cyan and yellow, respectively. Isosurface = 4×10^{-4} e/Å³.

respectively, U_{diss}° (metal, bulk) is the standard dissolution potential of the bulk metal, and n is the number of electrons involved in the dissolution. For heteronuclear, both different metals are discussed at the same time, which are defined as $E_f = E_{total} - E_{N6V4} - E_{M1} - E_{M2}$ and $U_{diss} = U_{diss}^{\circ}$(metal 1, bulk) + U_{diss}°(metal 2, bulk) $- \frac{E_f}{n1e + n2e}$.

In accordance with the definition provided in a previous study,[36] $E_f < 0$ eV indicated thermodynamical stability, while $U_{diss} > 0$ V versus the standard hydrogen electrode suggested electrochemical stability. The exact values of the E_f and U_{diss} of N6V4-M_2 and N6V4-M1M2 are listed in Tables S1 and S2, respectively.

The computed E_f values of nearly all of the selected N6V4-M_2/M1M2 systems, except for N6V4-Ag_2, are considerably below zero, suggesting the high thermodynamic stabilities of these metal dimers in the graphene-N6V4 substrate. With regard to U_{diss}, half-systems are excluded due to electrochemical instability under acidic conditions, as indicated by their negative U_{diss} values (Figure 2a).

Furthermore, attaining a low overpotential toward electrocatalytic CO_2RR is difficult due to adsorbate (particularly *COOH, *CO, and *CHO) scaling relations.[26,55,56] In general, the hydrogenation of *COOH to *CO or *CO to *CHO is always the potential rate-determining step (RDS) of CO_2 reduction, and thus, the overall catalytic efficiency depends on the binding energies of *COOH [E_b(COOH)], *CO [E_b(CO)], and *CHO [E_b(CHO)].[55] Accordingly, we then studied *CHO, *COOH, and *CO adsorption onto N6V4-M_2/M1M2. As shown in Figures 2b,c and S2, the scaling relations of the systems are completely different from those of pure metal surfaces. Points are dispersed in the entire region between E_b (COOH) and E_b (CO), proving that the diatomic systems can effectively break the traditional linear relationship. That is, for the same *COOH adsorption strength, DMACs have stronger *CO adsorption strength, making *COOH→*CO easier. Hence, forming *CO and approaching the desired low overpotential region are easier than the other hydrogenation steps. For the relationship between E_b (CHO) and E_b (CO), most systems exhibit a strong linear relationship, except for the six systems that

deviate significantly from the straight line, namely, N6V4-Pd_2, N6V4-Cr_2, N6V4-CrCo, N6V4-AgCr, N6V4-AgPd, and N6V4-NiPd. However, N6V4-Cr_2 and N6V4-CrCo are excluded due to their unsatisfactory results in the preceding stability tests. Hence, we finally identified four systems, namely, N6V4-Pd_2, N6V4-AgCr, N6V4-AgPd, and N6V4-NiPd, that meet the stability criteria and break the aforementioned scaling relations for further investigations. We also calculated the projected density of states (PDOS) of four candidates after adsorbed with *CO and are shown in Figure S3. It can be seen clearly that there is strong bonding between the p-orbitals of carbon atoms of the adsorbed *CO and the d orbitals of dual metals at the region of −7 to −8.5 eV below the Fermi energy level. Also, the insert numbers of electrons obtained by *CO further demonstrated the strong interaction between the *CO and metal active sites.

3.2. Activation of CO_2. The activation of CO_2 onto the surface of catalysts is always the first step in electrocatalytic CO_2 reduction. The structures of CO_2-adsorbed N6V4-M_2/M1M2 (N6V4-Pd_2, N6V4-AgCr, N6V4-AgPd, and N6V4-NiPd) are illustrated in Figure 3. CO_2 is first adsorbed on two metal sites of all four candidates. After the optimization of these candidates, CO_2 is slightly far away from the surface and then leads to physical adsorption, except for N6V4-AgCr. The binding strength between CO_2 and N6V4-AgCr is extremely strong, with an adsorption energy of −0.91 eV, and the distance between CO_2 and the metal of N6V4-AgCr is 2.60 Å. Meanwhile, the others are physically adsorbed with less negative adsorption energies of −0.45, −0.47, and −0.21 eV and longer distance between CO_2 and the metal of 3.58, 3.57, and 3.33 Å for N6V4-Pd_2, N6V4-AgPd, and N6V4-NiPd, respectively. The charge density difference of N6V4-M_2/M1M2 with CO_2 adsorption is shown in Figure 3. A significant charge transfer can be observed between the anchored metal dimers and CO_2. All of these findings indicate that CO_2 molecules can be activated by metal dimers embedded into graphene-N6V4.

3.3. Entire Pathways for CO_2RR. We then explored CO_2RR pathways based on N6V4-Pd_2, N6V4-AgCr, N6V4-AgPd, and N6V4-NiPd. The four candidates possess the same reaction pathways (Figure 4). The detailed free-energy
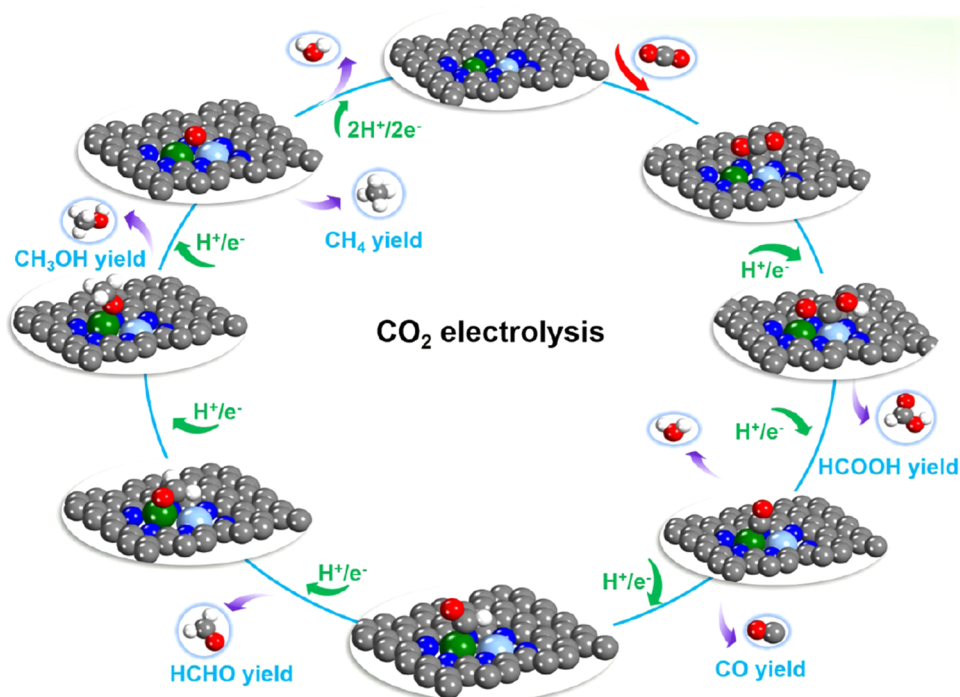
Figure 4. Comprehensive reaction network for the CO_2 reduction pathway toward a variety of C1 products, namely, CO, HCOOH, HCHO, CH_3OH, and CH_4, on N6V4-Pd_2, N6V4-AgCr, N6V4-AgPd, and N6V4-NiPd.

diagrams are shown in Figure 5, and the related optimized structures are shown in Figure S4.

The overall formula for the formation of each product is provided in the Supporting Information, i.e., eqs S1−S15. The dual-metal active centers significantly break the *CO−*CHO scaling relation; the RDS values of all of the candidates are not eq S8 [*CO + H^+ + e^- → *CHO (*COH) + H_2O], which is always the RDS for single-atom catalysts.[14,15] The production of CO occurs through the path of eq S4 [CO_2 → *COOH → CO]. The free energies of *CO_2 hydrogenation to form *COOH are increased by 0.78 eV (N6V4-AgPd), 0.38 eV (N6V4-AgCr), and 0.74 eV (N6V4-NiPd). This step is also the RDS for producing CH_4, and the corresponding overpotential is only 0.55 V for N6V4-AgCr, which is considerably lower than those of pure transition-metal surfaces (such as the theoretical overpotential on the Cu surface is 0.91 V).[57] However, the desorption of CO is found to be difficult for all of the candidates due to the strong adsorption. In the reaction pathway of eq S1, i.e., [CO_2 + $2H^+$ + $2e^-$ → HCOOH], CO_2 is hydrogenated by a proton−electron pair to form *COOH and then HCOOH generated via a second proton−electron pair transfers to *COOH. Only N6V4-AgPd is favorable for producing HCOOH, and the RDS is still the first hydrogenation of *CO_2 with a change of free energy of 0.78 eV, as shown in Figure 5c. The key step in the formation of deep reduction products with more than $2e^-$ reduction, namely, formaldehyde (HCHO), CH_3OH, and CH_4, is hydrogenation of *CO to form *CHO. However, the hydrogenation of *CO is not the RDS in our studied candidates due to the breaking of *CO−*CHO scaling relations. For N6V4-Pd_2 and N6V4-NiPd shown in Figure 5b,d, the hydrogenation of *CO is extremely easy with decreasing free energy. For the subsequent elementary reaction, i.e., eq S11 [*CHO + H^+ + e^- → *OCH_2 (*CHOH)], *CHO is hydrogenated to form *OCH_2 apart from *CHOH due to the relatively lower input energy for

*OCH_2 formation. Equation (11) is the energy consumption step for N6V4-Pd_2, with an increase of 0.59 eV free energy, and is also the RDS in the formation of the deep reduction product, namely, CH_3OH. However, the excessive binding strength between the intermediates and N6V4-Pd_2 leads to higher potentials for product desorption. *CHO hydrogenation on N6V4-NiPd is likely to proceed with eq S9 [*CHO + H^+ + e^- → HCHO] and HCHO as a final product (ΔG_{max} = 0.74 eV), as shown in Figure 5d. Then, the reaction proceeds with eq S12 [*OCH_2 + H^+ + e^- → *OCH_3], where the C atom becomes saturated, and the C−metal bond dissociates with the O atom that was directly connected at the bridge site of the metal dimer. The next proton−electron transfer leads to the dissociation of the C−O bond and the production of CH_4. In addition, the CO_2RR pathways to CH_4 are less competitive only for N6V4-AgCr due to the energetically disfavored intermediates along the reaction path toward its formation (Figure 5a). The introduction of AgCr dual-atom sites successfully reduces the change of free energy (ΔG) of *CO hydrogenation without increasing the ΔG of other elementary reactions. Therefore, breaking scaling relations by designing multiple active sites might be a universal method for catalyst development.

The thermodynamic limiting potentials toward C1 products, including CO, HCOOH, HCHO, CH_3OH, and CH_4, are summarized in Figure 5. The AgCr dimer exhibits much lower required potential toward CH_4 and HCOOH and higher potential toward other C1 products (Figure 5a). The proton−electron transfer of *COOH results in lower change of free energy (ΔG) of *CO hydrogenation without increasing ΔG, and the trend of HCOOH formation is upward. This finding indicates that the AgCr dimer exhibits higher efficiency and selectivity in generating CH_4. The limiting potentials toward all of the C1 products on the AgPd (0.78 eV) (Figure 5c) and NiPd (0.74 eV) (Figure 5d) dimers, which both occur during
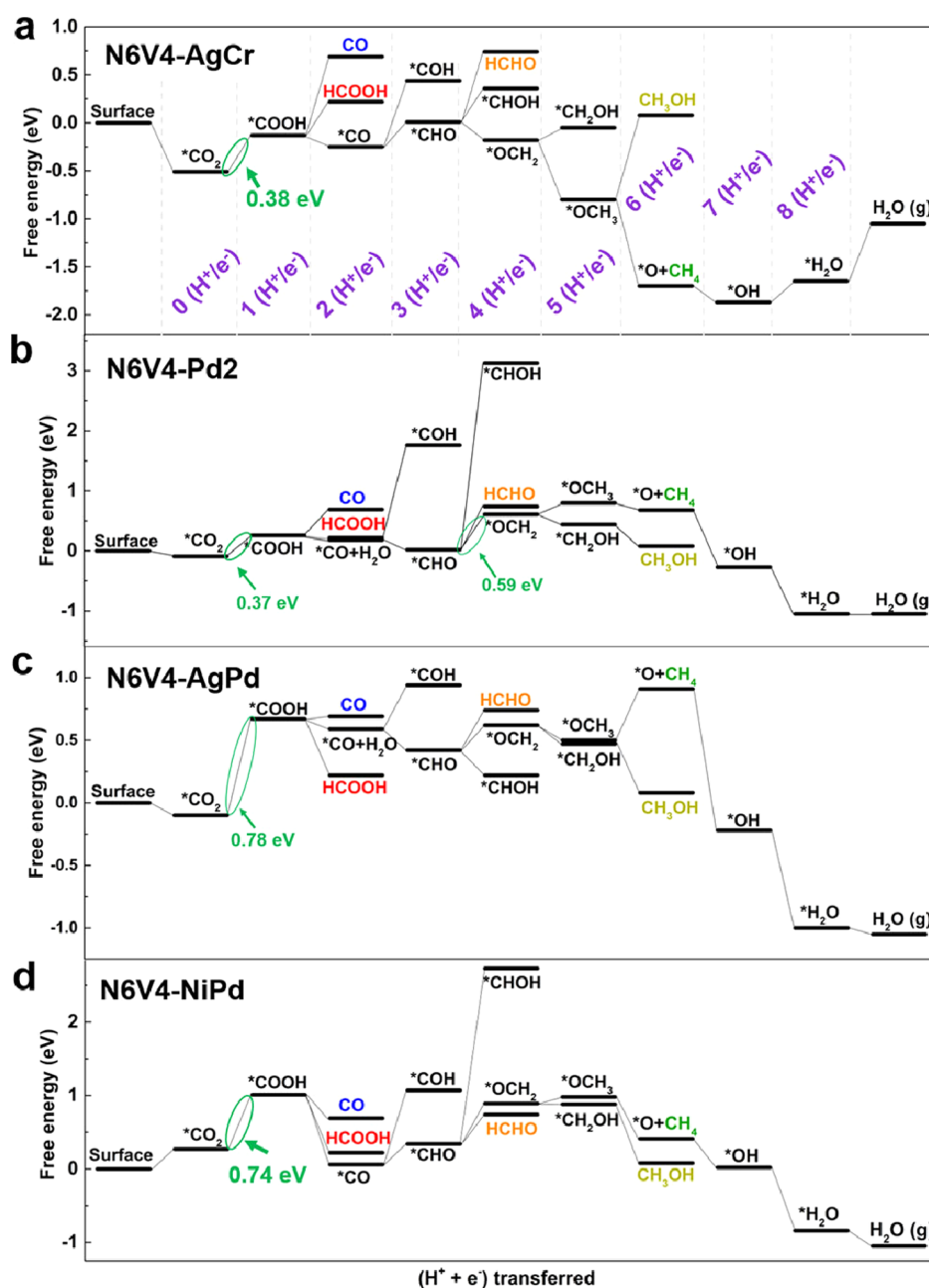
Figure 5. Free-energy profiles for the CO_2 reduction reaction to CO, HCOOH, HCHO, CH_4, and CH_3OH on (a) N6V4-AgCr, (b) N6V4-Pd2, (c) N6V4-AgPd, and (d) N6V4-NiPd at zero applied voltage (versus RHE).

the first hydrogenation (eq 2), are relatively high. Similar limiting potentials toward different products suggest poor selectivity. Meanwhile, the Pd_2 dimer exhibits relatively better selectivity toward the HCOOH product with a significantly low limiting potential (0.37 eV) (Figure 5b), while for deep reduction to produce CH_4, it exhibits lower efficiency and selectivity. We also calculated all reaction paths for CO_2 reduction to CH_4 of single-metal catalysts based on the candidates of dual-metal atom catalysts, including AgN_4, PdN_4, CrN_4, and NiN_4. The entire reaction path is shown in Figure S5. The CO_2 reduction performances of single sites are not good enough compared with that of dual metal sites, which show poor selectivity and high overpotentials. The limiting potentials for CrN_4, NiN_4, PdN_4, and AgN_4 are −0.71, −1.50, −1.78, and −2.01 eV, respectively. These results are all higher

than that of our corresponding dual-metal atoms in N-doped graphene (−0.38 eV for AgCr, −0.59 eV for Pd2, −0.78 eV for AgPd, and −0.74 eV for NiPd). It can also be seen from Figure S5 that the rate-determining steps all occur in the first hydrogenation step of the reaction process, except for CrN_4. The above results indicated that the activity of single sites in our work is not good enough compared with dual metal sites.

3.4. CO_2RR Versus HER. An ideal catalyst for CO_2RR, except high stability and activity, should also be able to effectively suppress HER to achieve high FE. Therefore, the next step is to judge the catalytic selectivity of the screened catalysts. In this context, we calculate the limiting potential between CO_2RR and HER $[U_L(CO_2RR) − U_L(HER)]$ to estimate the catalytic selectivity of different catalysts. The $U_L(CO_2RR) − U_L(HER)$ versus $U_L(CO_2RR)$ relationship of

the four promising CO_2RR catalysts is presented in Figure 6. The results indicate that N6V4-AgCr is located at the top right
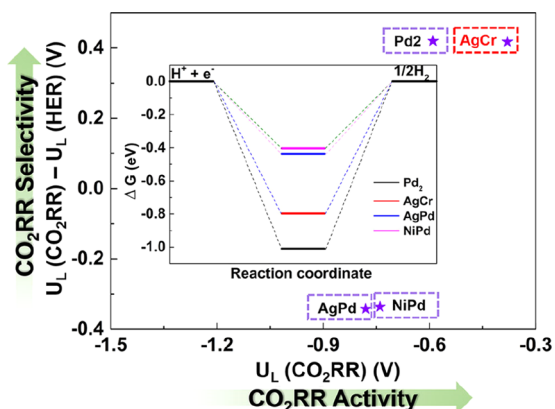

Figure 6. Limiting potential $[U_L(CO_2RR)]$ versus $U_L(CO_2RR) - U_L(HER)$, suggesting the CO_2RR activity and selectivity of the four screened catalysts. The inset in the figure shows the free-energy diagrams of HER.

corner of Figure 6, indicating its superior catalytic activity and excellent CO_2RR catalytic selectivity. Compared with the adsorption energy of *H on the metal site of N6V4-AgCr (−0.80 eV), CO_2 adsorption (−0.91 eV) is more negative. Consequently, the adsorption of CO_2 is preferred and the adsorption of H is hampered. However, N6V4-AgPd and N6V4-NiPd may not be favorable in the competition with H evolution, leading to poor CO_2RR selectivity. For N6V4-Pd$_2$, the adsorption energy of *H at the metal site (−1.00 eV) is more negative than that of *CO$_2$ (−0.45 eV), also indicating poor CO_2RR selectivity.

3.5. Activity Origin. What factor is responsible for the difference in dual-metal-dependent CO_2RR performance? To decode the underlying mechanism, electronic structures are analyzed by calculating the electron localized function (ELF)

and electrostatic potential (ESP) of the four candidates. In Figure S6, the ELF maps show that the electrons around C and N are highly localized and delocalized regions existing around metals. Therefore, the two metals in the middle can be inferred to be in the ionic state and a strong covalent bond is formed between C−N and C−C. The primary interaction between metal ions and N atoms is Coulombic attraction, which can be inferred from the lone pair between the metal ions and the N atoms (the red regions). Furthermore, the classic Lewis acid− base could be found at the metal ions and adjunct N, while the metals and their para-N atom (the green arrow in Figure 7a− d) show a distance from 4.169 to 4.556 Å. Because two metal atoms of the dual-atomic systems are out of the substrate, the interaction between metal and their para-N atom is regarded as delivering FLP-like activity (as shown by the green arrow in Figure 7a−d.). The electron transfer between CO_2 and Lewis pairs contributes to the Lewis acid activity of Lewis pairs.[58,59] Obviously, the bond lengths of Ag−N and Cr−N in N6V4-AgCr are 4.556 and 4.177 Å, respectively. Meanwhile, the bond lengths of Ag−N and Pd−N in N6V4-AgPd, Ni−N, and Pd− N in N6V4-NiPd and Pd1-N(Pd2-N) in N6V4-Pd2 are 4.350, 4.437, 4.387, 4.252, and 4.169(4.303) Å, respectively. In a nutshell, we can arrive at a conclusion that the enhanced acidity and basicity of Lewis sites, together with the elongated distance of Lewis pairs (Ag···N, 4.556 Å), contribute to the highest CO_2RR activity. The associative activation of CO_2 on FLPs leads to adsorption and hydrogenated pathway $[(*CO_2)-\delta^- + (H^+)\delta^+ + e^- \rightarrow *COOH]$ with moderate adsorption and low activation energy of 0.38 eV on N6V4-AgCr.

Although FLPs exist in all dual-metal candidates, the activity of FLPs also varies in different diatomic systems due to the difference in the d-orbital electronic arrangement of various transition metals. Figure 7 clearly shows the ESP distribution on different atoms. The reddish region has a lower ESP and is more susceptible to attacks by electrophilic reagents. The blue area has a high ESP and is susceptible to nucleophilic reagent assault. Nearly all of the N atoms are red, indicating low ESP. Compared with N6V4-Pd2, N6V4-AgPd, and N6V4-NiPd, the
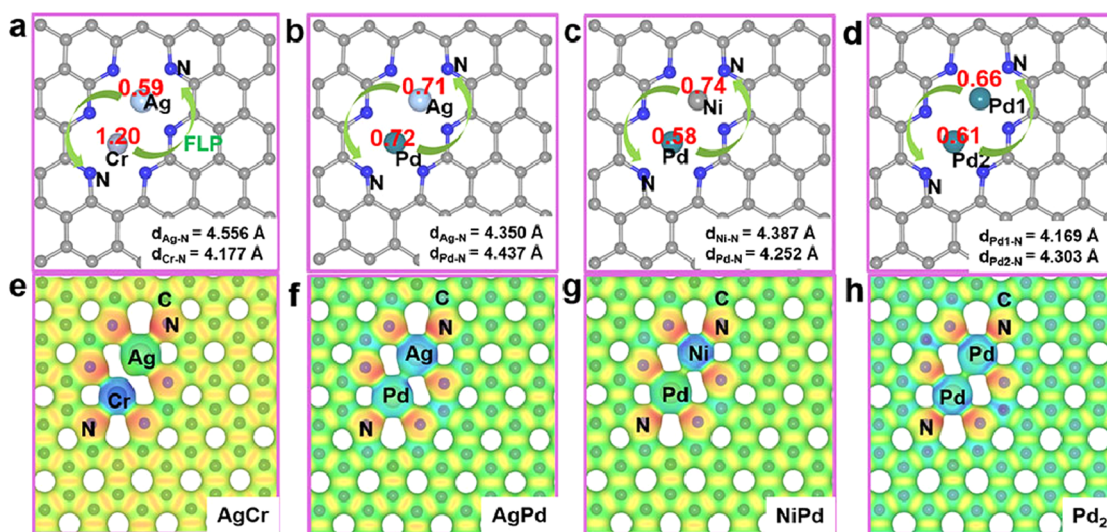

Figure 7. Schematic of the design concept for FLPs in the N6V4-M1M2/M$_2$ crystal structure. (a−d) Optimized structures of N6V4-Pd$_2$, N6V4-AgCr, N6V4-AgPd, and N6V4-NiPd. The red number indicates the lost Bader charge for each metal. (e−h) Corresponding electron density of the four candidates. Electron density isosurfaces are plotted at 0.07 e/bohr^3. The reddish region has a lower electrostatic potential and is more susceptible to attacks by electrophilic reagents. The bluer the area, the higher the ESP, and the easier it will be for nucleophilic reagents to attack the area.
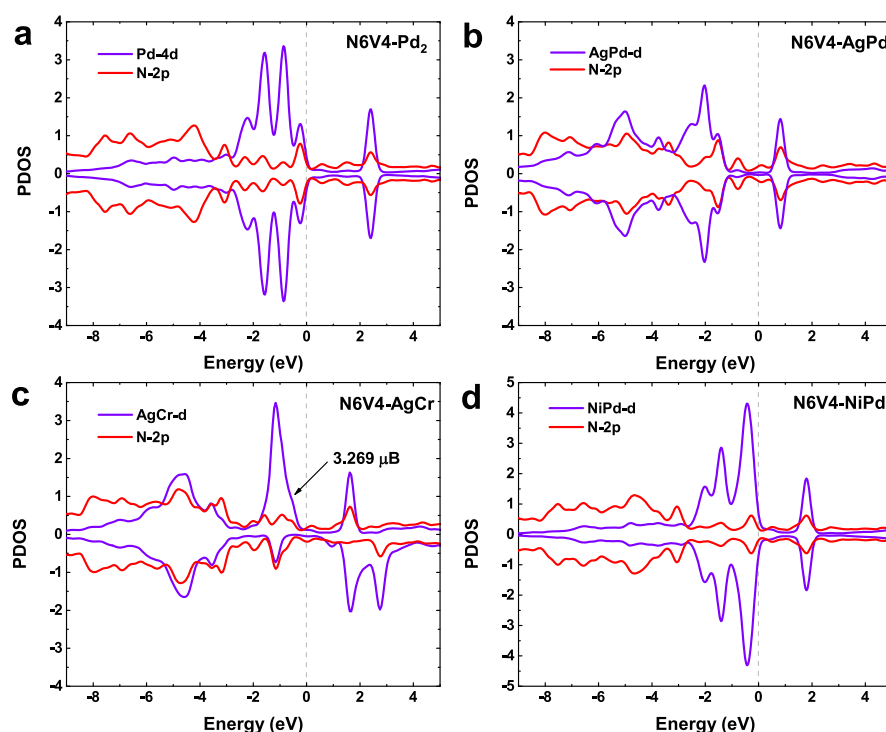
Figure 8. Partial density of states (PDOS) of metals and N on (a) N6V4-Pd$_2$, (b) N6V4-AgPd, (c) N6V4-AgCr, and (d) N6V4-NiPd before the adsorption of CO2. Fermi level is set to 0 eV.
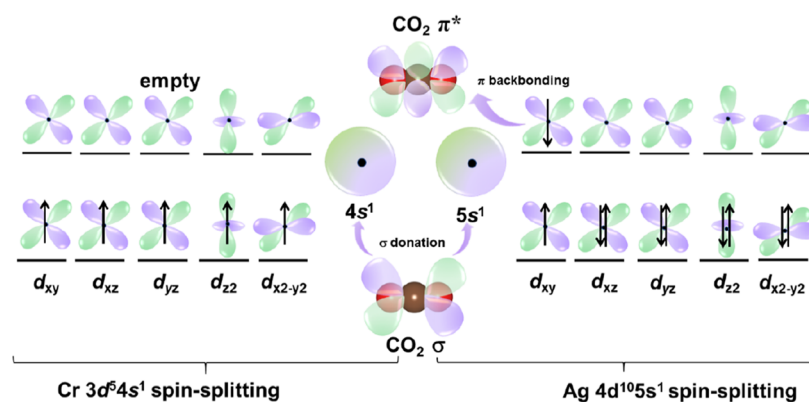

Figure 9. Electronic configurations of spin-split d orbitals for Cr and Ag to generate the empty spin-down higher-energy d orbitals of Cr or all fully spin-up and partially spin-down d orbitals of Ag, respectively. The arrows along different directions represent electrons with opposite spins. The CO$_2$ in the middle shows the relationship between the bonding state and the antibonding state of CO$_2$ and the outermost electrons of the metal.

Ag atom of N6V4-AgCr demonstrates a stronger charge contraction by adjacent Cr cations because the d orbital of Cr is in a semifull state, and thus, losing electrons is easier than that in the fully charged state of the d orbital of Ag. Bader charge analysis further indicates that the Ag of N6V4-AgCr is positively charged by approximately $0.59e^-$ loss and Cr shows a higher positive charge ($1.20e^-$) than all other metal atoms, suggesting higher capability to activate CO$_2$ molecules.[60]

3.6. d-Orbital Spin-Split Rule. To reveal the internal mechanism of the above results, the projected density of states (PDOS) of the above four candidates was compared (Figure 8). Previous studies have mentioned that spin polarization of transition metals will affect the adsorption of small molecules.[61,62] For example, the interaction of surface Mn atoms makes it produce strong spin polarization, which promotes the breaking of the N−N triple bond and subsequent reactions.[61] In addition, the spin polarization (1.38, 2.18, 1.07,

2.05, and 2.85 μB for Nb, Mo, Ta, W, and Re on g-CN, respectively) is obviously quenched after N$_2$ adsorption, promoting the activation of N$_2$.[62] In our case, activation of the CO$_2$ molecules is the first step of the CO$_2$RR. CO$_2$ consists of two σ bonds (generated from the sp hybrid orbital of the carbon atom and the p orbital of oxygen) and two delocalized π bonds (two p-orbitals of carbon atoms that are not involved in the hybridization overlap with p-orbitals of oxygen atoms side by side). Since the oxygen atom has a high electronegativity, the electron reactivity of the two pairs of highest occupied orbitals is strong, resulting in low chemical activity of the CO$_2$ molecule. By forming chemical bonds between CO$_2$ and the active sites of the catalyst, electrocatalysts stabilize CO$_2$ radicals or intermediates, resulting in a lower redox potential.[63] Furthermore, since CO$_2$ has an empty orbit with a lower energy level and a higher electron affinity, it accepts electrons easily.[64] Therefore, a catalyst with a strong ability to

lose electrons will aid the adsorption and activation of CO_2. The spin polarization (3.269 μB) is obviously seen only for N6V4-AgCr, promoting the activation of CO_2,[62] while no spin polarization is observed on N6V4-AgPd, N6V4-NiPd, and N6V4-Pd$_2$. We further calculated the PDOS of the entire stable diatomic structure combined with Ag, as shown in Figure S7. It revealed that the degree of electron spin polarization gradually decreases as the atomic number increases, such as the spin polarization of N6V4-AgCr is the largest (3.269 μB), while the spin polarizations of AgFe and AgCo gradually decrease to 1.848 and 0.590 μB, respectively. In comparison, AgNi, AgCu, and AgPd show high spin symmetry.

Furthermore, the local density of states (LDOS) is adopted to disclose the effect of the interaction between different metals on the spin polarization of d-orbital electrons compared with the bulk structure of each metal. Considering N6V4-AgCr as shown in Figure S8, the bulk structures of Ag and Cr metals show an octahedral coordination field in which d$_{xy}$, d$_{xz}$, and d$_{yz}$ triple-fold degenerated into one orbital, and d$_{x^2-y^2}$ and d$_{z^2}$ double-fold degenerated into another orbital alone. However, when Ag and Cr form a diatomic structure and coordinate with N, the degenerated d orbitals of Ag and Cr simultaneously split into five sub-bands of different energy levels and are accompanied by a peak shift. Upon polarization as shown in Figure 9, the d orbital produces five higher-energy spin-down d orbitals and five lower-energy spin-up orbitals. The electron arrangements of Cr are d^n = 5 with the outermost electron arrangement being 3d^{5}4s^1. Spin-up d orbitals are partially occupied (see Figure S8d for details), i.e., both the lowest unoccupied molecular orbital (LUMO) (around 1.8 eV) and highest occupied molecular orbital (HOMO) (around −1.5 eV) consist of spin-up d orbitals and leave the remaining spin-down d orbitals empty (from −3.5 to 1.8 eV), while the outermost electron arrangement of Ag is 4 d^{10}5s^1 and only the d$_{xy}$ orbital of Ag shows the spin polarization (see Figure S8b for details). Both spin-up and spin-down d$_{xy}$-orbitals occupied the LUMO (around 1−3 eV) and HOMO (around −2 to 0.5 eV), respectively. This result is also in agreement with the symmetry matching rule of the frontier orbitals of M-d and CO_2-σ/CO_2-π^*, which further illustrates the electron acceptance and donation as shown in Figure 9. N6V4-AgCr has more empty d orbitals and a high spin polarization to accept electrons and hence leads to the stronger CO_2 adsorption to initiate the reaction, while for AgPd (Figure S9), NiPd (Figure S10), and Pd$_2$ (Figure S11) diatomic structures, they will also lead to the splitting of the d orbital, but there is no spin polarization due to the higher occupations of d orbitals. Hence, CO_2 molecules will be favorably adsorbed onto the surface of N6V4-AgCr, and the subsequent hydrogenation processes, i.e., eqs S1−S13, will proceed successfully. Based on the above analysis, we found that the combination of different diatoms will lead to differences in the arrangement of metal d orbitals and this difference causes various electron spin polarizations and thus affects the selectivity and performance of catalysis.

4. CONCLUSIONS

In summary, we examined the potential of dual-metal atoms embedded into N-doped graphene, named N6V4-M$_2$ and N6V4-M1M2, as efficient CO_2RR electrocatalysts via high-throughput first-principles screening. We systematically studied 36 systems. Our results indicated that half-systems were first excluded as qualifying candidates that meet the screening criteria of thermodynamic and electrochemical stabilities.

Subsequently, only four systems were selected due to the significant deviations from linear scaling relations. Lastly, N6V4-AgCr was found to exhibit superior catalytic activity and selectivity toward CH_4 production with an extremely low overpotential of 0.55 V. Electronic structure analysis demonstrated that the FLPs formed between the metal and the para-N lead to a difference in the spin polarization of the systems, affecting catalytic performance. Overall, this work provides a comprehensive understanding for screening and designing novel DMACs with stability, activity, and selectivity. We believe this research will motivate additional experimental and theoretical studies to further explore ideal catalysts for CO_2 electroreduction.

■ ASSOCIATED CONTENT

Ⓢ Supporting Information

The Supporting Information is available free of charge at https://pubs.acs.org/doi/10.1021/acs.jpcc.0c10802.

Additional computational details; representative pathways of each product; optimized structures of all systems; value of formation energy and dissolution potential for all systems; and density of states of four candidates (PDF)

■ AUTHOR INFORMATION

Corresponding Authors

Lei Li − Hefei National Laboratory for Physical Sciences at the Microscale, Collaborative Innovation Center of Chemistry for Energy Materials, University of Science and Technology of China, Hefei 230026, P. R. China; Email: uestclilei@163.com

Kwan San Hui − School of Engineering, Faculty of Science, University of East Anglia, Norwich NR4 7TJ, United Kingdom; ⓞ orcid.org/0000-0001-7089-7587; Email: k.hui@uea.ac.uk

Fuming Chen − Guangdong Provincial Key Laboratory of Quantum Engineering and Quantum Materials, School of Physics and Telecommunication Engineering, South China Normal University, Guangdong 510006, P. R. China; ⓞ orcid.org/0000-0002-0108-9831; Email: fmchen@m.scnu.edu.cn

Kwun Nam Hui − Joint Key Laboratory of the Ministry of Education, Institute of Applied Physics and Materials Engineering, University of Macau, Taipa 999078, Macau SAR, P. R. China; ⓞ orcid.org/0000-0002-3008-8571; Email: bizhui@um.edu.mo

Authors

Shuo Wang − Joint Key Laboratory of the Ministry of Education, Institute of Applied Physics and Materials Engineering, University of Macau, Taipa 999078, Macau SAR, P. R. China

Jing Li − Joint Key Laboratory of the Ministry of Education, Institute of Applied Physics and Materials Engineering, University of Macau, Taipa 999078, Macau SAR, P. R. China

Chengzong Yuan − Joint Key Laboratory of the Ministry of Education, Institute of Applied Physics and Materials Engineering, University of Macau, Taipa 999078, Macau SAR, P. R. China

Yao Kang − Joint Key Laboratory of the Ministry of Education, Institute of Applied Physics and Materials Engineering,

University of Macau, Taipa 999078, Macau SAR, P. R. China

Jintao Zhang − *School of Chemistry and Chemical Engineering, Shandong University, Jinan 250100, P. R. China;* orcid.org/0000-0002-1029-3404

Feng Bin − *State Key Laboratory of High-Temperature Gas Dynamics, Institute of Mechanics, Chinese Academy of Sciences, Beijing 100190, P. R. China*

Xi Fan − *Ningbo Institute of Materials Technology, Engineering, Chinese Academy of Sciences, Ningbo 315201, P. R. China*

Complete contact information is available at:
https://pubs.acs.org/10.1021/acs.jpcc.0c10802

Notes
The authors declare no competing financial interest.

■ REFERENCES

(1) Liu, M.; Pang, Y.; Zhang, B.; De Luna, P.; Voznyy, O.; Xu, J.; Zheng, X.; Dinh, C. T.; Fan, F.; Cao, C.; et al. Enhanced Electrocatalytic CO2 Reduction Via Field-Induced Reagent Concentration. *Nature* **2016**, *537*, 382−386.

(2) Voiry, D.; Shin, H. S.; Loh, K. P.; Chhowalla, M. Low-Dimensional Catalysts for Hydrogen Evolution and CO2 Reduction. *Nat. Rev. Chem.* **2018**, *2*, No. 0105.

(3) Sheng, W.; Kattel, S.; Yao, S.; Yan, B.; Liang, Z.; Hawxhurst, C. J.; Wu, Q.; Chen, J. G. Electrochemical Reduction of CO2 to Synthesis Gas with Controlled Co/H-2 Ratios. *Energy Environ. Sci.* **2017**, *10*, 1180−1185.

(4) Nielsen, D. U.; Hu, X.-M.; Daasbjerg, K.; Skrydstrup, T. Chemically and Electrochemically Catalysed Conversion of CO2 to Co with Follow-up Utilization to Value-Added Chemicals. *Nat. Catal.* **2018**, *1*, 244−254.

(5) Zheng, X.; Ji, Y.; Tang, J.; Wang, J.; Liu, B.; Steinruck, H.-G.; Lim, K.; Li, Y.; Toney, M. F.; Chan, K.; et al. Theory-Guided Sn/Cu Alloying for Efficient CO2 Electroreduction at Low Overpotentials. *Nat. Catal.* **2019**, *2*, 55−61.

(6) Jiao, J. Q.; Lin, R.; Liu, S. J.; Cheong, W. C.; Zhang, C.; Chen, Z.; Pan, Y.; Tang, J. G.; Wu, K. L.; Hung, S. F.; et al. Copper Atom-Pair Catalyst Anchored on Alloy Nanowires for Selective and Efficient Electrochemical Reduction of CO2. *Nat. Chem.* **2019**, *11*, 222−228.

(7) Kuang, M.; Wang, Q. H.; Han, P.; Zheng, G. F. Cu, Co-Embedded N-Enriched Mesoporous Carbon for Efficient Oxygen Reduction and Hydrogen Evolution Reactions. *Adv. Energy Mater.* **2017**, *7*, No. 1700193.

(8) Wang, L. M.; Chen, W. L.; Zhang, D. D.; Du, Y. P.; Amal, R.; Qiao, S. Z.; Bf, J. W.; Yin, Z. Y. Surface Strategies for Catalytic CO2 Reduction: From Two-Dimensional Materials to Nanoclusters to Single Atoms. *Chem. Soc. Rev.* **2019**, *48*, 5310−5349.

(9) Fan, K.; Jia, Y. F.; Ji, Y. F.; Kuang, P. Y.; Zhu, B. C.; Liu, X. Y.; Yu, J. G. Curved Surface Boosts Electrochemical CO2 Reduction to

Formate Via Bismuth Nanotubes in a Wide Potential Window. *ACS Catal.* **2020**, *10*, 358−364.

(10) Nitopi, S.; Bertheussen, E.; Scott, S. B.; Liu, X.; Engstfeld, A. K.; Horch, S.; Seger, B.; Stephens, I. E. L.; Chan, K.; Hahn, C.; et al. Progress and Perspectives of Electrochemical CO2 Reduction on Copper in Aqueous Electrolyte. *Chem. Rev.* **2019**, *119*, 7610−7672.

(11) Xu, S.; Carter, E. A. Theoretical Insights into Heterogeneous (Photo)Electrochemical CO2 Reduction. *Chem. Rev.* **2019**, *119*, 6631−6669.

(12) Li, F.; Li, Y. C.; Wang, Z.; Li, J.; Nam, D.-H.; Lum, Y.; Luo, M.; Wang, X.; Ozden, A.; Hung, S.-F.; et al. Cooperative CO2-to-Ethanol Conversion Via Enriched Intermediates at Molecule−Metal Catalyst Interfaces. *Nat. Catal.* **2020**, *3*, 75−82.

(13) Wang, W.; Qu, Z.; Song, L.; Fu, Q. CO2 Hydrogenation to Methanol over Cu/Ceo2 and Cu/Zro2 Catalysts: Tuning Methanol Selectivity Via Metal-Support Interaction. *J. Energy Chem.* **2020**, *40*, 22−30.

(14) Abild-Pedersen, F.; Greeley, J.; Studt, F.; Rossmeisl, J.; Munter, T. R.; Moses, P. G.; Skulason, E.; Bligaard, T.; Norskov, J. K. Scaling Properties of Adsorption Energies for Hydrogen-Containing Molecules on Transition-Metal Surfaces. *Phys. Rev. Lett.* **2007**, *99*, No. 016105.

(15) Calle-Vallejo, F.; Loffreda, D.; Koper, M. T. M.; Sautet, P. Introducing Structural Sensitivity into Adsorption-Energy Scaling Relations by Means of Coordination Numbers. *Nat. Chem.* **2015**, *7*, 403−410.

(16) Kuhl, K. P.; Cave, E. R.; Abram, D. N.; Jaramillo, T. F. New Insights into the Electrochemical Reduction of Carbon Dioxide on Metallic Copper Surfaces. *Energy Environ. Sci.* **2012**, *5*, 7050−7059.

(17) Whipple, D. T.; Kenis, P. J. A. Prospects of CO2 Utilization Via Direct Heterogeneous Electrochemical Reduction. *J. Phys. Chem. Lett.* **2010**, *1*, 3451−3458.

(18) Ooka, H.; Figueiredo, M. C.; Koper, M. T. M. Competition between Hydrogen Evolution and Carbon Dioxide Reduction on Copper Electrodes in Mildly Acidic Media. *Langmuir* **2017**, *33*, 9307−9313.

(19) Li, L.; Li, B.; Guo, H.; Li, Y.; Sun, C.; Tian, Z.; Chen, L. Synergistic Effects of Heteroatom-Decorated Mxene Catalysts for Co Reduction Reactions. *Nanoscale* **2020**, *12*, 15880−15887.

(20) Li, L.; Wang, X.; Guo, H.; Yao, G.; Yu, H.; Tian, Z.; Li, B.; Chen, L. Theoretical Screening of Single Transition Metal Atoms Embedded in Mxene Defects as Superior Electrocatalyst of Nitrogen Reduction Reaction. *Small Methods* **2019**, *3*, No. 1900337.

(21) Liu, L.; Corma, A. Metal Catalysts for Heterogeneous Catalysis: From Single Atoms to Nanoclusters and Nanoparticles. *Chem. Rev.* **2018**, *118*, 4981−5079.

(22) Liu, J.-C.; Xiao, H.; Li, J. Constructing High-Loading Single-Atom/Cluster Catalysts Via an Electrochemical Potential Window Strategy. *J. Am. Chem. Soc.* **2020**, *142*, 3375−3383.

(23) Yang, X.-F.; Wang, A.; Qiao, B.; Li, J.; Liu, J.; Zhang, T. Single-Atom Catalysts: A New Frontier in Heterogeneous Catalysis. *Acc. Chem. Res.* **2013**, *46*, 1740−1748.

(24) Zhong, M.; Tran, K.; Min, Y.; Wang, C.; Wang, Z.; Dinh, C. T.; De Luna, P.; Yu, Z.; Rasouli, A. S.; Brodersen, P.; et al. Accelerated Discovery of CO2 Electrocatalysts Using Active Machine Learning. *Nature* **2020**, *581*, 178−183.

(25) Huang, Q.; Liu, H.; An, W.; Wang, Y.; Feng, Y.; Men, Y. Synergy of a Metallic Nico Dimer Anchored on a C2n−Graphene Matrix Promotes the Electrochemical CO2 Reduction Reaction. *ACS Sustainable Chem. Eng.* **2019**, *7*, 19113−19121.

(26) Ouyang, Y.; Shi, L.; Bai, X.; Li, Q.; Wang, J. Breaking Scaling Relations for Efficient CO2 Electrochemical Reduction through Dual-Atom Catalysts. *Chem. Sci.* **2020**, *11*, 1807−1813.

(27) Li, R.; Wei, Z.; Gou, X. Nitrogen and Phosphorus Dual-Doped Graphene/Carbon Nanosheets as Bifunctional Electrocatalysts for Oxygen Reduction and Evolution. *ACS Catal.* **2015**, *5*, 4133−4142.

(28) Li, Z.; He, H.; Cao, H.; Sun, S.; Diao, W.; Gao, D.; Lu, P.; Zhang, S.; Guo, Z.; Li, M.; et al. Atomic Co/Ni Dual Sites and Co/Ni Alloy Nanoparticles in N-Doped Porous Janus-Like Carbon Frame-

works for Bifunctional Oxygen Electrocatalysis. *Appl. Catal., B* **2019**, *240*, 112−121.

(29) Zheng, Y.; Jiao, Y.; Zhu, Y.; Cai, Q.; Vasileff, A.; Li, L. H.; Han, Y.; Chen, Y.; Qiao, S. Z. Molecule-Level G-C3n4 Coordinated Transition Metals as a New Class of Electrocatalysts for Oxygen Electrode Reactions. *J. Am. Chem. Soc.* **2017**, *139*, 3336−3339.

(30) Wang, J.; Gan, L.; Zhang, W.; Peng, Y.; Yu, H.; Yan, Q.; Xia, X.; Wang, X. In Situ Formation of Molecular Ni-Fe Active Sites on Heteroatom-Doped Graphene as a Heterogeneous Electrocatalyst toward Oxygen Evolution. *Sci. Adv.* **2018**, *4*, No. eaap7970.

(31) Jia, C.; Ren, W.; Chen, X.; Yang, W.; Zhao, C. (N, B) Dual Heteroatom-Doped Hierarchical Porous Carbon Framework for Efficient Electroreduction of Carbon Dioxide. *ACS Sustainable Chem. Eng.* **2020**, *8*, 6003−6010.

(32) Li, Y.; Chen, C.; Cao, R.; Pan, Z.; He, H.; Zhou, K. Dual-Atom Ag-2/Graphene Catalyst for Efficient Electroreduction of CO2 to Co. *Appl. Catal., B* **2020**, *268*, No. 15809.

(33) Zhao, J.; Zhao, J.; Li, F.; Chen, Z. Copper Dimer Supported on a C2n Layer as an Efficient Electrocatalyst for CO2 Reduction Reaction: A Computational Study. *J. Phys. Chem. C* **2018**, *122*, 19712−19721.

(34) Luo, G.; Jing, Y.; Li, Y. Rational Design of Dual-Metal-Site Catalysts for Electroreduction of Carbon Dioxide. *J. Mater. Chem. A* **2020**, *8*, 15809−15815.

(35) Li, H.; Zhao, Z.; Cai, Q.; Yin, L.; Zhao, J. Nitrogen Electroreduction Performance of Transition Metal Dimers Embedded into N-Doped Graphene: A Theoretical Prediction. *J. Mater. Chem. A* **2020**, *8*, 4533−4543.

(36) Guo, X.; Gu, J.; Lin, S.; Zhang, S.; Chen, Z.; Huang, S. Tackling the Activity and Selectivity Challenges of Electrocatalysts toward the Nitrogen Reduction Reaction Via Atomically Dispersed Biatom Catalysts. *J. Am. Chem. Soc.* **2020**, *142*, 5709−5721.

(37) Zhang, X.; Chen, A.; Zhang, Z.; Zhou, Z. Double-Atom Catalysts: Transition Metal Dimer-Anchored C2n Monolayers as N2 Fixation Electrocatalysts. *J. Mater. Chem. A* **2018**, *6*, 18599−18604.

(38) He, Z.; He, K.; Robertson, A. W.; Kirkland, A. I.; Kim, D.; Ihm, J.; Yoon, E.; Lee, G.-D.; Warner, J. H. Atomic Structure and Dynamics of Metal Dopant Pairs in Graphene. *Nano Lett.* **2014**, *14*, 3766−3772.

(39) Wang, J.; Huang, Z.; Liu, W.; Chang, C.; Tang, H.; Li, Z.; Chen, W.; Jia, C.; Yao, T.; Wei, S.; et al. Design of N-Coordinated Dual-Metal Sites: A Stable and Active Pt-Free Catalyst for Acidic Oxygen Reduction Reaction. *J. Am. Chem. Soc.* **2017**, *139*, 17281−17284.

(40) Wang, Q.; Ji, Y.; Lei, Y.; Wang, Y.; Wang, Y.; Li, Y.; Wang, S. Pyridinic-N-Dominated Doped Defective Graphene as a Superior Oxygen Electrocatalyst for Ultrahigh-Energy-Density Zn-Air Batteries. *ACS Energy Lett.* **2018**, *3*, 1183−1191.

(41) Wang, Y.; Han, P.; Lv, X.; Zhang, L.; Zheng, G. Defect and Interface Engineering for Aqueous Electrocatalytic CO2 Reduction. *Joule* **2018**, *2*, 2551−2582.

(42) Ye, W.; Chen, S.; Lin, Y.; Yang, L.; Chen, S.; Zheng, X.; Qi, Z.; Wang, C.; Long, R.; Chen, M.; et al. Precisely Tuning the Number of Fe Atoms in Clusters on N-Doped Carbon toward Acidic Oxygen Reduction Reaction. *Chem* **2019**, *5*, 2865−2878.

(43) Zhou, P.; Hou, X.; Chao, Y.; Yang, W.; Zhang, W.; Mu, Z.; Lai, J.; Lv, F.; Yang, K.; Liu, Y.; et al. Synergetic Interaction between Neighboring Platinum and Ruthenium Monomers Boosts Co Oxidation. *Chem. Sci.* **2019**, *10*, 5898−5905.

(44) Ren, W.; Tan, X.; Yang, W.; Jia, C.; Xu, S.; Wang, K.; Smith, S. C.; Zhao, C. Isolated Diatomic Ni-Fe Metal-Nitrogen Sites for Synergistic Electroreduction of CO2. *Angew. Chem., Int. Ed.* **2019**, *58*, 6972−6976.

(45) Grimme, S. Semiempirical Gga-Type Density Functional Constructed with a Long-Range Dispersion Correction. *J. Comput. Chem.* **2006**, *27*, 1787−1799.

(46) Kresse, G.; Furthmuller, J. Efficient Iterative Schemes for Ab Initio Total-Energy Calculations Using a Plane-Wave Basis Set. *Phys. Rev. B* **1996**, *S4*, 11169−11186.

(47) Perdew, J. P.; Burke, K.; Ernzerhof, M. Generalized Gradient Approximation Made Simple. *Phys. Rev. Lett.* **1996**, *77*, 3865−3868.

(48) Perdew, J. P.; Wang, Y. Pair-Distribution Function and Its Coupling-Constant Average for the Spin-Polarized Electron Gas. *Phys. Rev. B* **1992**, *46*, 12947−12954.

(49) Blöchl, P. E. Projector Augmented-Ware Method. *Phys. Rev. B* **1994**, *50*, No. 17953.

(50) Monkhorst, H. J.; Pack, J. D. Special Points for Brillouin-zone integrations. *Phys. Rev. B* **1976**, *13*, 5188−5192.

(51) Grimme, S.; Antony, J.; Ehrlich, S.; Krieg, H. A Consistent and Accurate Ab Initio Parametrization of Density Functional Dispersion Correction (Dft-D) for the 94 Elements H-Pu. *J. Chem. Phys.* **2010**, *132*, No. 154104.

(52) Grimme, S.; Ehrlich, S.; Goerigk, L. Effect of the Damping Function in Dispersion Corrected Density Functional Theory. *J. Comput. Chem.* **2011**, *32*, 1456−1465.

(53) Li, Q.-K.; Li, X.-F.; Zhang, G.; Jiang, J. Cooperative Spin Transition of Monodispersed Fen3 Sites within Graphene Induced by Co Adsorption. *J. Am. Chem. Soc.* **2018**, *140*, 15149−15152.

(54) Greeley, J.; Norskov, J. K. Electrochemical Dissolution of Surface Alloys in Acids: Thermodynamic Trends from First-Principles Calculations. *Electrochim. Acta* **2007**, *52*, 5829−5836.

(55) Shi, C.; Hansen, H. A.; Lausche, A. C.; Norskov, J. K. Trends in Electrochemical CO2 Reduction Activity for Open and Close-Packed Metal Surfaces. *Phys. Chem. Chem. Phys.* **2014**, *16*, 4720−4727.

(56) Hansen, H. A.; Varley, J. B.; Peterson, A. A.; Norskov, J. K. Understanding Trends in the Electrocatalytic Activity of Metals and Enzymes for CO2 Reduction to Co. *J. Phys. Chem. Lett.* **2013**, *4*, 388−392.

(57) Li, Y.; Sun, Q. Recent Advances in Breaking Scaling Relations for Effective Electrochemical Conversion of CO2. *Adv. Energy Mater.* **2016**, *6*, No. 1600463.

(58) Liu, L.; Lukose, B.; Ensing, B. A Free Energy Landscape of CO2 Capture by Frustrated Lewis Pairs. *ACS Catal.* **2018**, *8*, 3376−3381.

(59) Zhang, S.; Huang, Z. Q.; Ma, Y.; Gao, W.; Li, J.; Cao, F.; Li, L.; Chang, C. R.; Qu, Y. Solid Frustrated-Lewis-Pair Catalysts Constructed by Regulations on Surface Defects of Porous Nanorods of Ceo2. *Nat. Commun.* **2017**, *8*, No. 15266.

(60) Chen, S.; Yuan, H.; Morozov, S. I.; Ge, L.; Li, L.; Xu, L.; Goddard, W. A. Design of a Graphene Nitrene Two-Dimensional Catalyst Heterostructure Providing a Well-Defined Site Accommodating One to Three Metals, with Application to CO2 Reduction Electrocatalysis for the Two-Metal Case. *J. Phys. Chem. Lett.* **2020**, *11*, 2541−2549.

(61) Wang, S.; Li, B.; Li, L.; Tian, Z.; Zhang, Q.; Chen, L.; Zeng, X. C. Highly Efficient N-2 Fixation Catalysts: Transition-Metal Carbides M2c (Mxenes). *Nanoscale* **2020**, *12*, 538−547.

(62) Niu, H.; Wang, X.; Shao, C.; Zhang, Z.; Guo, Y. Computational Screening Single-Atom Catalysts Supported on G-Cn for N2 Reduction: High Activity and Selectivity. *ACS Sustainable Chem. Eng.* **2020**, *8*, 13749−13758.

(63) Chen, S.; Wang, H.; Kang, Z.; Jin, S.; Zhang, X.; Zheng, X.; Qi, Z.; Zhu, J.; Pan, B.; Xie, Y. Oxygen Vacancy Associated Single-Electron Transfer for Photofixation of CO2 to Long-Chain Chemicals. *Nat. Commun.* **2019**, *10*, No. 788.

(64) Kong, Y.; Liu, D.; Ai, H.; Lo, K. H.; Wang, S.; Pan, H. Theoretical Screening of Single Atoms Supported on Two-Dimensional Nb2cn2 for Nitrogen Fixation. *ACS Appl. Nano Mater.* **2020**, *3*, 11274−11281.